PHYSICAL REVIEW APPLIED **20,** 044004 (2023)

Nonlocal metasurface based on the multiport structural model

Jie Ren and Zhilin Hou[*]
School of Physics and Optoelectronics, South China University of Technology, Guangzhou 510640, China

(Received 28 May 2023; revised 22 August 2023; accepted 14 September 2023; published 3 October 2023)

Recent progress on metasurfaces has revealed the nonlocal features of this kind of multiunit artificial structure. It has been shown that there is always intercoupling between the constituent units, which must be considered in their design. Such an intercoupling makes the design process difficult, especially when the number of constituent units becomes large. We show in this paper that a metasurface can be generally described by a multiport structural model, based on which an efficient design method can be established. To show the main idea of the model and the adaptability of the method based on it, nonlocal metastructures with various target fields, including an anomalous reflector, mode convertor in waveguide, wave focuser, and structure for a bound state in a continuum are designed. The successfully designed metastructures show that the suggested method is generally valid for structures with various target fields and is also efficient enough for structures with a large number of constituent units. The model gives not only an efficient method for designing metasurfaces, but also a general understanding of metastructures, based on which nonlocal metastructures for field control in complex environments, such as in organic tissue and architectural structures, can be expected.

DOI: 10.1103/PhysRevApplied.20.044004

I. INTRODUCTION

Highly efficient wave manipulation via artificial structures is greatly desired in the materials physics and engineering communities. As thin compact structures, acoustic metasurfaces have attracted significant attention in recent years because of their unique properties and capabilities in controlling and transforming wave fronts [1]. Many fascinating and exotic properties, such as anomalous refraction and reflection [2–4], asymmetric transmission [5–7], focusing [8–10], acoustic cloaking [11–13], and acoustic holography [14,15], have been realized by use of such inhomogeneous two-dimensional (2D) artificial structures.

The devices designed to realize those properties and physical effects are mostly constructed according to the generalized Snell's law (GSL) [16]. For acoustic waves, a typical structure based on this principle is the planar anomalous reflector [4], which is designed to reflect a plane wave from the direction with incident angle θ_i into the direction with a reflective angle $\theta_r (\neq \theta_i)$. As has been shown in Ref. [4], to design such a structure we first need to obtain a position-dependent phase difference $\Phi(x)$ along the surface direction x, so that the condition $k_0 \sin\theta_r = k_0 \sin\theta_i + (d\Phi(x)/dx)$ can be satisfied, where k_0 is the wave vector. This step can be done according to the analytical expression of the incident and desired reflective waves. After this step, constituent units with a substructure that can realize the phase jump $\Phi(x)$ at different values of x are accordingly designed. It can be found from the method that the constituent units at different values of x relate only to the local $\Phi(x)$ and can be individually designed. Therefore, we refer to the device based on the principle as the local structure.

However, further investigations have shown that the local structure usually has the intrinsic problem of low efficiency [17], especially for structures designed for large $d\Phi(x)/dx$. To understand the underlying physics, the power-flow-conservation law in a wave reflection procedure was checked in Ref. [18]. It was shown that, for a reflector with planar surface, when $\theta_r \neq \theta_i$ is required, the surface-normal component of the local intensity of the total field varies from positive to negative values along the surface, while the integration over the periods $[x + na, x + (n + 1)a]$ is zero, where x is any position on the surface, n is an integer, and $a = 2\pi/(k_0|\sin\theta_r - \sin\theta_i|)$. This means a lateral energy exchange along the surface direction must be considered if we try to transfer perfectly the incident energy into the target field via a passive structure. To design such a device, the constituent units in each period need to be designed cooperatively rather than independently. To emphasize the fact that the constituent units cannot be designed individually from the local $\Phi(x)$ obtained in the method based on the GSL framework, we refer to this kind of structure as a nonlocal metasurface. It is obvious that this is a common feature of most metastructures because a metastructure is usually designed to steer the wave front into an

---

[*] phzlhou@scut.edu.cn

© 2023 American Physical Society

anomalous direction, and the power-flow-conservation law in the surface-normal direction cannot usually be locally satisfied.

Up to now, various methods have been suggested to design nonlocal metasurfaces [19–22]. For example, Epstein and Eleftheriades have shown in Ref. [22] that the lateral energy exchange can be realized by an explicitly introduced auxiliary evanescent wave on the surface, and the constituent units can then be independently designed based on the total field including the auxiliary one. Meanwhile, Diaz-Rubio *et al*. have shown in Ref. [23] that the power-flow-conservation condition along the surface-normal direction can be locally satisfied on a so-called power-flow-conformal (PFC) surface, on which the constructive units can be individually designed. In these methods, the authors designed the metasurfaces by first balancing the surface-normal-direction power flow on a local position along the surface, upon which the subunits can be individually constructed. However, it would be a challenge to extend these methods for general use because, for the former method, the analytical form of such an evanescent mode could exist only in a system with a surface of a special shape, while for the latter method, the obtained PFC surface would mostly be a curved surface in an unexpected shape. Alternatively, Ni *et al.* have shown in Ref. [21] that a highly efficient metasurface can be obtained by optimizing a procedure based on the mode-matching method, and Fan and Mei have shown in Ref. [24] that a direct structural optimizing algorithm based on the finite-element method (FEM) can also be used for such a design. In these methods, a numerical method for wave scattering behavior is established, based on which the desired structure can be selected by an optimization algorithm. However, it can be found in the design procedure that the scattering behavior for systems with different configurations must be solved many times in the optimizing procedure. Because the computation time of the numerical method for determining the wave scattering behavior increases as the size of the system becomes larger and larger, these methods would be time consuming if they were extended for structures with large numbers of constituent units.

We notice that, although metasurfaces achieve their ability to control wave fronts via subwavelength units placed on a surface, it is the strong near-field interaction between the constituent units that plays the key role, while what we really care about is in fact their far-field property. In this sense, we can treat a metasurface generally as a closed system with a number of ports; inputs from the ports in the far field can be input into and scattered away from the system. Under this model, the metastructure design can be understood as a procedure of customizing the output mode in one or several given ports under the known inputs from all ports. Because the output mode in each port is the superposition of the scattered waves excited by all incidences, the desired output modes in given ports can be obtained either by changing the scattering property of the system or by adjusting the incidences in the ports, or by changing both. From this view of point, it can be found that the previously suggested design methods are based mostly on the first idea, i.e., changing the configuration of the constituent units so that the scattering property of the system is changed. Because the exact relationship between the scattering property and the configuration of constituent units can only be obtained by solving the wave equation, this kind of method means solving the wave equation many times while searching for the desired structure, which inevitably results in a time-consuming calculation. In this paper, we show that the output mode in one or several given ports can also be customized by changing only the inputs from the ports. We show that besides the regular ports occupied by the external inputs and the customized outputs, we can introduce a sufficient number of additional ports in which the incident waves can be treated as the reflection of the scattered waves in themselves, and a passive metastructure can then be designed by adjusting the reflective property at their far ends.

We point out that the suggested method can greatly reduce the design complexity of the metastructure. To show the main idea of the model and the efficiency and adaptability of the method based on it, metastructures with various target fields, including a metasurface for anomalous reflection, mode converter in a waveguide, highly efficient planar focuser, and coupled cavities in open space for a bound state in a continuum (BIC) are designed. From the successfully designed structures, we can see that the suggested method is simple and generally valid for structures with various target fields, and more importantly, it is also efficient enough for structures with a large number of constituent units, which can hardly be done by the methods reported in previous works.

It is necessary to point out that our model gives not only an efficient method for metasurface design, but also an alternative understanding of metastructures. Compared to the understanding from the GSL and grating theory, based on which the metasurfaces are mainly designed to deflect the wave front, the multiport structural model understands the metasurface from the principle of superposition, based on which nonlocal metastructures for field control in complex environments, such as in organic tissue, architectural structures, etc., can be expected.

The paper is organized as follows. After the introduction, in Sec. II we take the design of a 2D anomalous reflector as example to give the general idea of the method. In Sec. III we present three examples to show the adaptability of the method for structures with different target fields. Section IV is the conclusion of the work.

II. THE GENERAL IDEA OF THE METHOD BASED ON THE MODEL

To demonstrate how the multiport structural model works, we first adapt it to design a metagrating [21] for anomalous reflection as example. For simplicity, we consider only a simple metagrating designed to reflect a normally incident plane wave into the direction with reflection angle θ_r. According to the grating theory, for a periodically structured surface with pitch a_0, the wave solution in the half-infinite space above the surface will take the form of an infinite summation of the Floquet-Bloch modes, with $G_n = n(2\pi/a_0)$, $(n = 0, \pm 1, \ldots, \pm\infty)$ as the Fourier spectrum of the nth-order mode. By setting the pitch as $a_0 = \lambda_0/\sin\theta_r$, where λ_0 is the wavelength of the incident wave, we can obtain the propagating constant of the nth-order mode as $\beta_n = (2\pi/\lambda_0)\sqrt{1-(n\sin\theta_r)^2}$, which will take real values only for $n = 0$ and ± 1 as $\theta_r > (\pi/6)$. This means there are three possible propagating modes in the upper half-infinite space using this setting. That is to say, the plane wave incident from the surface-normal direction (or from $\pm\theta_r$ directions) could only be reflected in three possible directions in the far field. In this sense, we say that there are three ports in the upper half-infinite space that can support the real incident and reflected Floquet-Bloch modes.

In Fig. 1(a) we show schematically a periodically structured surface with pitch a_0, in which three possible incident and reflective directions are labeled as port 1 to port 3. To realize the anomalous reflection, we need to add N waveguides per unit cell in the lower half-infinite space of the surface as additional ports, which is shown schematically in Fig. 1(b) ($N = 2$ is shown in the figure). From these additional ports, waves can also be injected into the system. For such a system, the total scattered wave in any port should be the superposition of the scattered waves excited by the input from all ports. In the following design, we set the width of the added waveguides to be the same and to be smaller than $\lambda_0/2$, so that only the zeroth-order waveguide mode can exist. This means there is only one port in

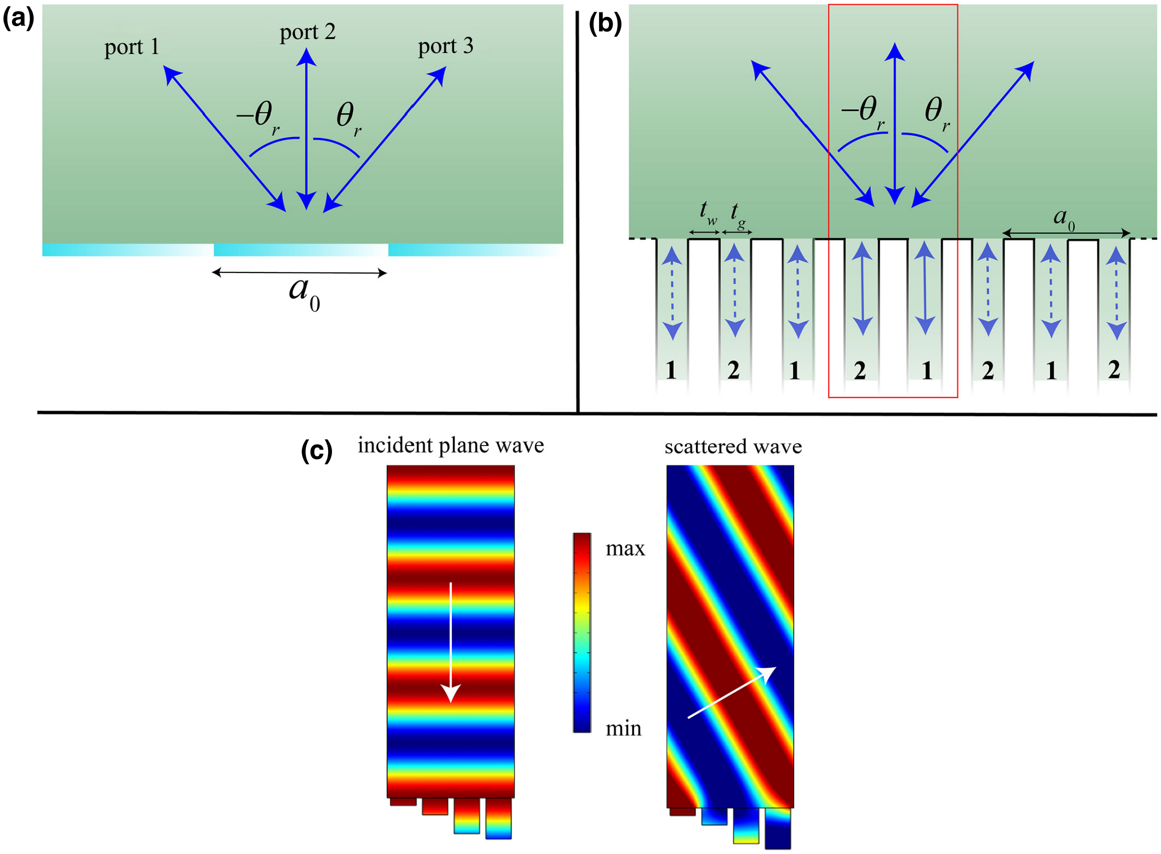

FIG. 1. (a) Schematic view of a reflective metagrating with pitch $a_0 = \lambda_0/\sin\theta_r$. The incident plane wave from directions with angle $-\theta_r$, 0, and θ_r can only be reflected back as plane waves along $-\theta_r$, 0, or θ_r directions according to the grating theory. We denote these channels as port 1, port 2, and port 3, respectively. (b) A multiport structural model with two additional waveguides (i.e., ports) per unit cell. The unit cell is marked out by a box in red. t_g and t_w denote the width of the waveguides and the wall thickness between the nearest neighbors, respectively. (c) Field distribution of the real part of the pressure wave for a designed structure. The left and right panel are for the incident and reflected waves, respectively; the propagating direction of the plane wave is shown by arrows in white.

each waveguide. Notice that this is just for simplicity and not necessary in principle.

For notation convenience, we separate the ports into two subsets, which are those in the upper half-infinite space and those in the waveguides. We denote the amplitude of the wave modes in the ports (ports 1 to 3) in the upper half-infinite space by $A^{\pm} = (A_1^{\pm}, A_2^{\pm}, A_3^{\pm})^T$, while we denote the amplitude of waves in the N added waveguides (i.e., the additional ports) by $H^{\pm} = (H_1^{\pm}, \ldots, H_N^{\pm})$, respectively, where the superscript $+$ $(-)$ means the wave into (away from) the structure. Under this notation, the reflection and transmission in ports in the upper half-infinite free space and in the waveguides can be, respectively, expressed as

$$A^- = R^A A^+ + T^H H^+, \tag{1}$$

and

$$H^- = T^A A^+ + R^H H^+. \tag{2}$$

In Eq. (1), the matrix element $R_{ij}^A (i,j = 1,2,3)$ describes the reflective coefficient in port i when the incident wave is from port j in the upper half-infinite space, while $T_{ij}^H (i = 1,2,3;\ j = 1,\ldots,N)$ describes the scattering coefficient in port i in the upper half-infinite space when the incident wave is from the additional port j in the waveguide. Similarly, in Eq. (2), matrix element $T_{ij}^A (i = 1,\ldots,N;\ j = 1,2,3)$ means the transmission coefficient in the additional port i in the waveguide when the incident wave is from port j in the upper half-infinite space, and $R_{ij}^H (i,j = 1,\ldots,N)$ means the reflective coefficient in the additional port i when the incident wave is from the additional port j in the waveguide.

To design a passive reflector, we need to set $A_i^+ = A_0 \delta_{i,2}, (i = 1,2,3)$ and $H_j^+ = r_j H_j^-, (j = 1,\ldots,N)$, where δ_{ij} is a Dirac delta function. This means that, except for the only independent incident wave from port 2, the incidence H_j^+ from the jth port $(j = 1,\ldots,N)$ is just the reflection of H_j^- with a complex reflection coefficient r_j $(|r_j| \leq 1$ is required for a passive structure). Under this restriction, Eq. (2) can be rewritten as

$$(R^H - R^W)H^+ = -T^A A^+, \tag{3}$$

where R^W is a diagonal matrix with elements $R_{ij}^W = (1/r_j)\delta_{ij}$.

By combining Eqs. (1) and (3), we can eliminate H^+ and then solve A^- for a given A^+ and R^W. In the design of the passive anomalous reflector, we can end the jth waveguides with length l_j by a sound-hard boundary for simplicity, under which we have $r_j = e^{i2k_0 l_j}$, where k_0 is the wave vector, and the design can be implemented by searching l_j for the maximum $|A_3^-|$ using an optimization algorithm.

As an illustration, we show in Fig. 1(c) the field distribution of the reflected wave from the designed structure with $\theta_r = 60^\circ$ under normal incidence. The real part of the pressure field in one unit cell is given. In the design, we use a total of $N = 4$ waveguides per unit cell, and the width of each waveguide is set to be $0.2a_0$, while the thickness of the wall between the nearest waveguides is set as $0.05a_0$. Under this setting, the depths of the four waveguides are found by the optimization algorithm to be $0.069\lambda_0$, $0.155\lambda_0$, $0.326\lambda_0$, and $0.377\lambda_0$, respectively, for the case shown in Fig. 1(c). To check the energy transfer efficiency of the obtained structure, we calculate the total power flow in the surface-normal direction of the reflective wave in one period, and find that the normally incident wave energy is transferred almost completely into the desired direction.

To obtain the matrices R^A, T^A, R^H, and T^H in Eqs. (1) and (3), we can use a numerical method based on analytical formulas if the wave solution in the upper half-infinite space and in all additional ports have an analytical form, like the ones presented in Refs. [21,25]. Generally, they can be obtained by numerical simulation, or even by experimental measurement. To test the adaptability of our method, we use the FEM supplied by COMSOL Multiphysics to calculate these matrices in the present and following examples. For the structure shown in Fig. 1(b), we use the Floquet boundary condition on the left and right boundaries of the unit cell (marked by a red box in the figure), and perfectly matching layers are added on the top of the unit cell and at the far end of the waveguides to mimic the nonreflective boundary. To calculate the matrix elements R_{ij}^A and T_{ij}^A, a plane wave with unit amplitude is input from the upper half-infinite space with incident angle $-\theta_r$, 0, and θ_r, which correspond to the ports in the upper half-infinite space indexed by $j = 1, 2$, and 3, and the scattered waves in all ports are then measured. Amplitudes of the reflected positive and negative first- and zeroth-order Floquet-Bloch modes in the upper half-infinite space, which are extracted by the Fourier transformation from the scattering wave distribution, provide the elements ofR_{ij}^A, while the amplitude of the zeroth-order mode in the jth waveguide provides the elements of T_{ij}^A. The calculations for matrix elements R_{ij}^H and T_{ij}^H are similar, but use the incident wave from the jth waveguide in the simulation, instead.

For this and for the following example structures, we use the acoustic pressure module in the COMSOL Multiphysics software to do the numerical simulation. In the COMSOL model, no viscous effect is considered, and the interfaces between the medium and waveguides are set to be sound hard. The working medium is air with mass density $\rho = 1.28$ kg/m^3 and wave velocity $v = 343$ m/s. The matrices are extracted using a homemade code based on COMSOL with MATLAB, and the optimization is finished by the genetic algorithm supplied by MATLAB.

It is necessary to point out that, compared with methods suggested in Refs. [21,24], our method can greatly reduce the design complexity. In these previously suggested methods, to search for the desired structure using the genetic algorithm, the wave scattering behavior, or the scattering matrix, needs to be calculated for all individuals in each recursive step in the optimization procedure. However, in our method, the matrices R^A, T^A, R^H, and T^H only need to be calculated once, and the optimization for l_j is based on the linear equation presented in Eq. (3), which has only the same order as the number of waveguides.

To show the efficiency of the suggested method, we count the CPU time for the matrix calculation and for the optimization procedure, and compare them with those for the methods given in Refs. [21,24]. For our method, the absolute CPU time for matrix calculation is about 24 s, and for the optimization it is about 0.3 s on a machine with Intel(R) Xeon(R) Platinum 8160 CPU × 2 and 1 Tbyte of RAM, while for the method given in Refs. [21,24], the optimization time for the same system is about 77.2 s and 3.3 h, respectively, using the same machine. Notice that the CPU time presented here is just for comparison; the absolute value is less meaningful because it relates strongly to the mesh size in the FEM calculation and the truncating terms in the mode-matching method, and the optimization time of the genetic algorithm depends on the population size and the initialization. To give a relatively fair comparison, all the CPU times listed here are counted under the minimum requirement of the parameters necessary for numerical convergence.

III. DESIGNING EXAMPLE STRUCTURES WITH VARIOUS TARGET FIELDS

In this section, we take the design of three structures, i.e., the mode convertor in a waveguide, the planar focuser, and the structure for a BIC as examples to show the generality of the suggested model and the adaptability of the method based on it. These three examples are typical structures with different target fields. In contrast to the anomalous reflector presented previously, which has a target field of Floquet-Bloch form in upper half-infinite space, the target field for the mode convertor is the Fourier mode in a confined space, and the target field for planar focuser is the wave field distribution in real space, while for the BIC structure, null far-field radiation is the design target. Similar structures have been understood from different aspects and designed by different methods, but structures with full consideration of nonlocal effects are still lacking. We show in the following that they are necessary and can all be designed by the suggested method.

A. Mode conversion in a waveguide

Mode conversion in a waveguide has been studied for both electromagnetic (EM) and acoustic waves [7,26–29] because it relates to the concept of one-way transmission. It has been shown that a directional dependent energy response can be achieved by such structures even under time-reversal symmetry, which would be practically useful in controlling wave fronts.

Among those studies, structures with a slab of gradient-index metamaterial (GIM) decorated on the inner walls of the waveguide have been suggested for both EM [27,29] and acoustic [28] waves. In these structures, the decorated wall will act as a GSL-based anomalous reflector that can reflect the incident wave from the θ_i direction into the θ_r ($\neq \theta_i$) direction [27]. Consequently, it can be predicted that after several reflections in the waveguide, waves propagating along (against) the length direction will be converted into surface waves (reflected back) [27,28]. Based on this mechanism, structures for asymmetric transmission and mode conversion can be designed [27–29]. However, it can be found that the index of the GIM layer in these structures is commonly set to vary slowly in the length direction, which results a relatively long device (for example, it is about $7.6\lambda_0$ in Ref. [27]). We point out that this is necessary because we must reserve enough space for a sufficient number of structured subunits to realize the required gradient index. From this point, we conclude that a compact and simultaneously highly efficient mode convertor, which would be necessary in some practical cases, would be a difficult task for this method. However, as we have pointed out in Refs. [20,21], by introducing a strong intercoupling between the neighboring subunits, or say by introducing a nonlocal effect into the design procedure, a compact structure with fewer subunits can be expected. In the following, we show that such a device falls into our multiport structural model, and a highly efficient and compact structure can be designed accordingly.

As a demonstration, we design two 2D structures that can realize the functionalities shown in Fig. 2(a). For both of these, we consider a 2D main waveguide with width $\lambda_0/2 < h_0 < \lambda_0$, in which the zeroth- and first-order waveguide modes can coexist. As is shown schematically in the upper panel of Fig. 2(a), the first function to be realized is the transformation of the incident zeroth-order mode from area $A1$ into the first-order mode in area $A3$, and at the same time, the first-order mode can also be transformed from $A1$ into the zeroth-mode in $A3$. The second function to be realized is the transformation of the zeroth-order incident mode from $A1$ to the first-order mode in $A3$, while the first-order mode from $A1$ and the zeroth-order mode from $A3$ will be totally reflected simultaneously. This is the exact one-way transmission reported in Refs. [7,26–28] because the zeroth-order incidence from the left- and right-hand sides of the main waveguide results in a completely different energy response. The functionality of this device is shown schematically in the lower panel of Fig. 2(a).

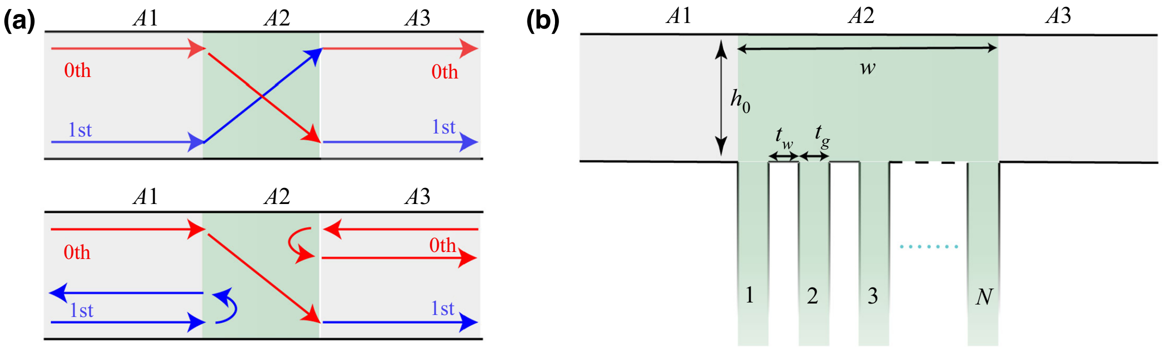

FIG. 2. (a) Mode conversion in waveguide. The upper and lower panel show schematically the functionalities of mode conversion to be realized. Arrows in color show the propagating direction of the wave modes. The conversion is finished in area $A2$ where the metastructure is built. (b) The multiport structural model in area $A2$. h_0 is the height of the main waveguide, w is the total width of area A2, t_g is the width of the subwaveguides, and t_w is the thickness of the wall between the nearest subwaveguides.

To design these structures, we consider the corresponding multiport structure shown schematically in Fig. 2(b). For the structure, the zeroth- or first-order mode can input into (or output away from) the system either from $A1$ or from $A3$, which means there are four ports in the main waveguide. Taking a similar notation to that used in the design shown in the previous section, we denote the amplitude of the modes in the main waveguide as $A^{\pm} = (A_1^{\pm}, \ldots, A_4^{\pm})$. Part $A2$ is the area in which the mode conversion will be finished. It has a width of w and is decorated by N subwaveguides from the lower boundary. By letting the width of these subwaveguides be smaller than $\lambda_0/2$, and denoting the amplitude of the input and output modes in them as $H^{\pm} = (H_1^{\pm}, \ldots, H_N^{\pm})$, we can calculate the matrices R^A, T^A, R^H, and T^H, and then the scattering amplitude A^- can be customized by optimizing the ending length $l_j\,(j = 1, \ldots, N)$ of these subwaveguides according to Eqs. (1) and (3).

For the first functionality shown schematically in the upper panel in Fig. 2(a), we choose $h_0 = 0.8\lambda_0$, $w = 1.15\lambda_0$, and $N = 6$, the widths of the subwaveguides are all set to be $0.15\lambda_0$, and the wall thickness between the nearest neighbor is set to be $0.05\lambda_0$. Under these settings, the optimized ending lengths of the subwaveguides are obtained as $0.138\lambda_0$, $0.161\lambda_0$, $0.109\lambda_0$, $0.122\lambda_0$, $0.169\lambda_0$, and $0.147\lambda_0$, respectively. To check the performance of the obtained structure, we calculate the energy transforming ratio between the incident and desired mode as the function of λ/λ_0, where λ is the wavelength of the incident wave in free space. The results are shown in Fig. 3(a), in which the red curve is for the first- to zeroth-order mode, while the black curve is for the zeroth- to first-order mode. It can be seen from the figure that these two curves almost overlap, both of them become unity at $\lambda/\lambda_0 = 1$, and keep a value larger than 0.8 when λ/λ_0 stays in the range $0.96 - 1.07$. It can be seen that the bandwidth is narrow because the structure is designed only for $\lambda = \lambda_0$. To give a direct demonstration of the functionality, the field distribution of the real part of the pressure wave for $\lambda = \lambda_0$ is shown in Fig. 3(b), in which the upper panel is for the transformation from zeroth- to first-order mode, while the lower panel is for first to zeroth-order mode. Notice that the length of the structure for an EM wave with similar function reported in Ref. [29] is about $7.6\lambda_0$, which is much longer than the one suggested here.

For the second functionality shown schematically in the lower panel in Fig. 2(a), we choose $w = 2\lambda_0$ and $N = 10$, while t_g, t_w, and h_0 are the same as for the system in the upper panel. Under these parameters, the optimized ending lengths of the subwaveguides are obtained respectively as $0.223\lambda_0$, $0.137\lambda_0$, $0.196\lambda_0$, $0.118\lambda_0$, $0.259\lambda_0$, $0.262\lambda_0$, $0.120\lambda_0$, $0.135\lambda_0$, $0.167\lambda_0$, and $0.144\lambda_0$. To check the performance of the obtained structure, we calculate the transmission behavior of the incidences from area $A1$. Shown in Fig. 3(c) are the energy transmission coefficients as a function of λ/λ_0, where λ is the wavelength of the incident wave in free space, and the transmission coefficient is defined as the total energy flow of the transmitted waves over that for the single incident mode. In the figure, the red curve is for the zeroth-order incident mode, while the curve in black is for the first-order incident mode. Notice that, according to the time-reversal law, the black (red) curve also represents the transmission coefficient for the zeroth-order (first-order) incident mode from $A3$. It can be seen from the figure that the asymmetric transmission behavior occurs throughout the considered frequency range, and the perfect asymmetric transmission appears at the exact point with $\lambda = \lambda_0$. To give a direct illustration of the functionality, we show in Fig. 3(d) the field distribution of the real part of the scattered pressure wave for incidence from area $A1$ with $\lambda = \lambda_0$, in which the upper panel is for the zeroth-order incident mode, while the lower panel is for the first-order incident mode. Notice that the field of the incident mode is not shown in Fig. 3(d).

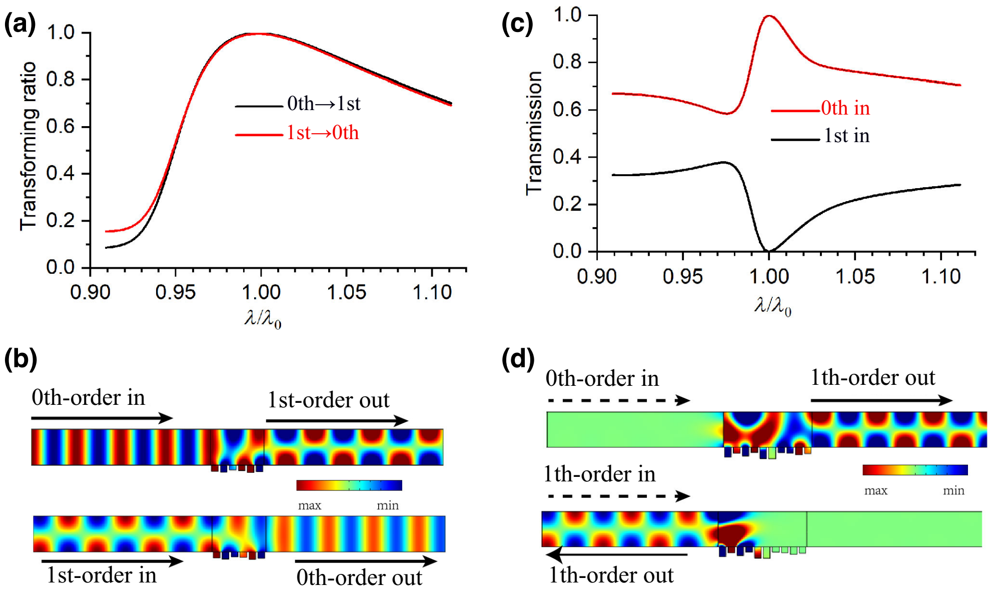

FIG. 3. (a) Energy transforming ratio between the incident and desired modes as a function of working wavelength in the designed structure with the functionality shown in the upper panel of Fig. 2(a): red curve is the transformation from first- to zeroth-order mode; black curve is for zeroth- to first-order mode. (b) Field distribution of the pressure wave at $\lambda/\lambda_0 = 1$ in (a): arrows in black show the propagating direction of the wave. (c) Energy transmission coefficient as a function of working wavelength in the designed structure with the functionality shown in the lower panel of Fig. 2(a); red (black) curve is the transmission for zeroth-order (first-order) incidence from area $A1$. (d) Field distribution of the pressure wave at $\lambda/\lambda_0 = 1$ in (c); only the scattered field is shown.

B. Nonlocal planar focuser in uniform media

Planar metasurfaces for acoustic or elastic wave focusing have been reported by several groups [10,13,30,31]. The most reported structures are those based on the GSL theory [30], in which the constituent units are locally designed and the coupling between them is completely neglected. However, because a GSL-based structure suffers a problem of low efficiency when the steering angle is large, the wave energy at the far edges of the metasurface can hardly be deflected into the focus spot, so would have less contribution on the focusing effect, especially for a structure with a large numerical aperture. Recent research has shown that the focusing efficiency can be improved using a hybrid structure [10] or a PFC structure [13]. The key technique in these design methods is to introduce nonlocal elements into the structure, so that the wave energy impacting on the far edges of the structure can also be collected. Unfortunately, despite a considerable improvement in efficiency, the structures based on these methods can only partly consider the coupling between the constituent units, which prevents a further improvement in efficiency. We show here that, benefiting from the extremely reduced design complexity, our method can take a full consideration of the interunit coupling and a full nonlocal planar focuser can be designed, even when the number of the constituent units becomes large.

As is shown schematically in Fig. 4(a), we consider a 2D planar reflective focuser for acoustic waves. It has N grooves spanning from $-(a/2)$ to $a/2$ carved on a sound-hard surface, and the focal spot is set at the position of $(0,f)$. For simplicity, we restrict the width of the grooves to be narrower than $\lambda_0/2$, under which only the zeroth-order mode can exist in the grooves. The design purpose is to find a set of groove depths $\{l_j\}(j = 1, \ldots, N)$ with which the surface can reflect and focus an incident wave at $(0,f)$. To fulfill the task, we extend the N grooves in the structure as bottomless waveguides, and wave modes can input from their lower end toward the surface. Using this model, the matrices R^A, T^A, R^H, and T^H in Eqs. (1) and (3) can be calculated. For the present model, R^A needs to be defined as the amplitude of the scattering wave at the focal spot $(0, f)$ for the wave incident from the upper half-infinite space, while the jth element of the matrix T^H, say, T^H_j, needs to be defined as the amplitude of the scattering wave at the focal spot $(0, f)$ for the mode incident from the jth waveguide. The other two matrices, T^A and R^H, have the same definition as those in the previously mentioned examples. After the matrices are obtained, the depth of the grooves is found according to Eqs. (1) and (3) using an optimization algorithm with the maximum amplitude of the scattered wave at the focal spot as the target function.

As an example, we design a structure with $a = 30\lambda_0$ and $f = 2\lambda_0$. For simplicity, the grooves are arranged equidistantly on the surface with the same width of $t_g = 0.16\lambda_0$, and the wall thickness between the nearest grooves is set to be $t_w = 0.04\lambda_0$. Under this setting, $N = 150$ grooves are needed in the structure. For a normally incident plane wave, which is the case considered in our design, the

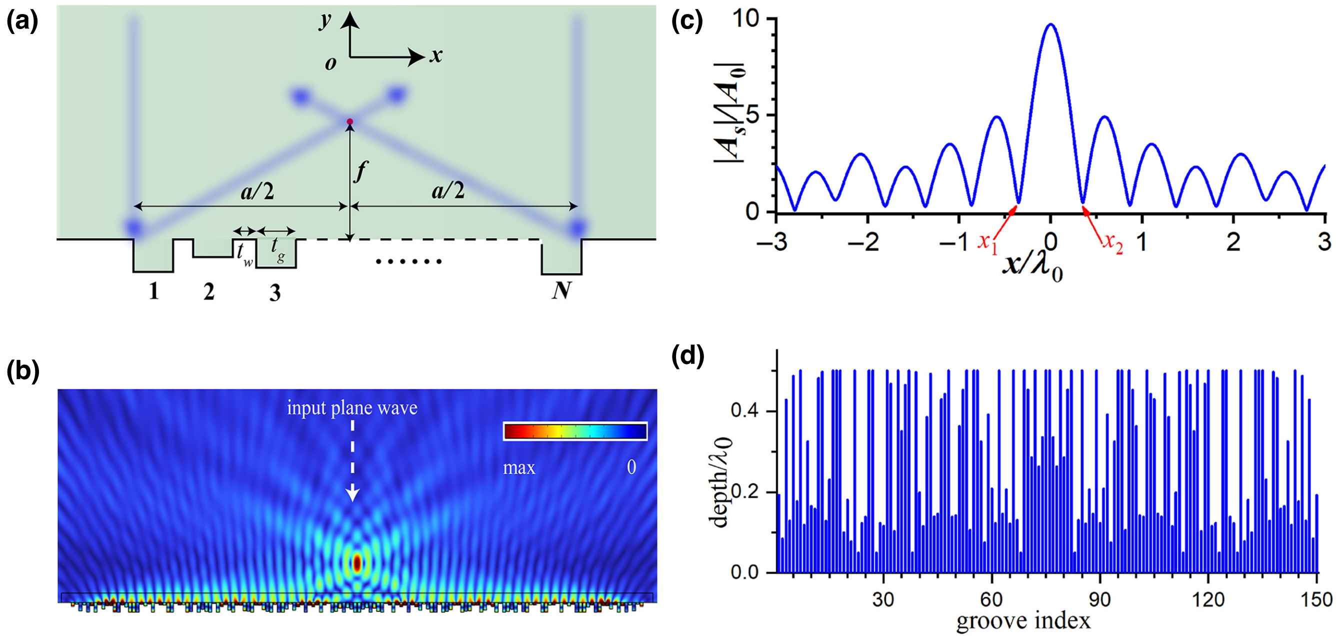

FIG. 4. (a) Two-dimensional focuser constructed by carving N grooves on a sound-hard planar surface. The grooves span from $x = -a/2$ to $a/2$ on the surface, the focal point is set at $(0, f)$. The blurred blue arrows show schematically the trajectory of the propagating wave. (b) Field distribution of the amplitude of the scattered pressure field for the designed structure with $a = 30\lambda_0$ and $f_0 = 2\lambda_0$. The normally incident plane wave is shown by a white arrow. (c) Amplitude distribution of the scattered wave on focal plane; only the field in the region of $(-3\lambda_0,\ 3\lambda_0)$ is shown, the value is normalized by the amplitude of the incident wave A_0. x_1 and x_2 mark the edges of the main peak. (d) The optimized depth of the grooves of the structure.

depths of only half of the grooves need to be optimized according to the symmetry property.

Shown in Fig. 4(b) is the amplitude field of the scattering pressure wave for the designed structure under the incidence with unit amplitude, and Fig. 4(c) shows the amplitude distribution of the scattering wave on the focal plane, which is shown as a ratio of $|A_s|/|A_0|$, where A_s and A_0 are the amplitude of the scattering and incident wave, respectively. The optimized depth of the grooves is shown in Fig. 4(d). To evaluate the focal quality of the structure, we define a Q factor as the ratio of the reflected power flow near the focal spot over the total incident power flow delivered to the structure, i.e., $Q = \int_{x_1}^{x_2} I_s(x)dx / \int_{-(a/2)}^{a/2} |I_0(x)|dx$, where $I_s(x)$ and $I_0(x)$ are the distribution of the y-directional intensity of the scattering and incident wave on the focal plane, respectively, and x_1, x_2 are the edge positions of the main focal peak [see Fig. 4(c)]. From the simulation result, we can find that the Q factor of the structure is $Q = 65.7\%$ with the width of the main peak being $\Delta x = x_2 - x_1 = 0.7\lambda_0$, and the maximum value of pressure amplitude at the focal spot is $|A_s|/|A_0| = 9.72$. Compared to the values for the corresponding GSL structure, which are $Q = 28.6\%$, $\Delta x = 0.67$, and $|A_s|/|A_0| = 6.90$, the focal quality of our nonlocal structure has been greatly improved. For the corresponding GSL structure for comparison, we use the ideal surface impedance calculated by $Z = Z_0(1 + e^{i\theta}/1 - e^{i\theta})$ with $\theta = k_0\left(\sqrt{|x|^2 - f^2} - f\right)$ in the numerical simulation [13]. Notice that the Q factor and the maximum value of the amplitude would be smaller if constituent subunits were used instead.

C. Structure for a bound state in a continuum

BICs are waves that remain localized even though they coexist with a continuous spectrum of radiating waves that can carry energy away. They are a general wave phenomenon and have been identified in EM waves [32], acoustic waves [33], water waves [34], and elastic waves [35]. Full discussion of the mechanism and potential application of BICs can be found in Refs. [36,37]. As the authors have summarized in these two review papers, BICs are mostly investigated in given structures as states due to symmetry or separability, or due to the destructive interference of resonances, while specifically engineered BICs achieved through inverse construction have rarely been reported, especially for acoustic or EM waves. Realizing a BIC system for classical waves through reverse engineering may offer a lot of promise for engineering.

We understand the BIC system as a nonlocal metastructure with null radiation but with strong intercoupling between subunits, and show in the following that a BIC system can be described by the multiport model and can be designed by our suggested method.

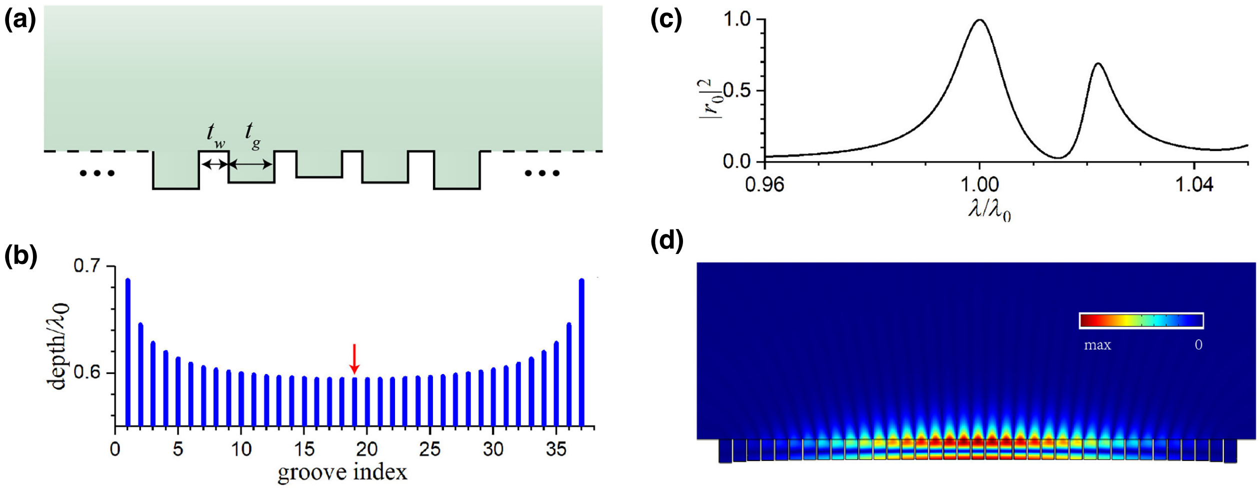

FIG. 5. (a) Structure for BIC with a sound-hard surface decorated by grooves from bottom. t_g and t_w denote, respectively, the width of the groove and the wall thickness between the nearest neighbors. (b) The depth of the grooves of the obtained structure: red arrow marks the central groove. (c) Reflective coefficient $|r_0|^2$ as function of λ/λ_0. Incidence is from the central groove marked by red arrow in (b); reflection is measured in the same groove. (d) Field distribution of the amplitude of the pressure wave; incidence is from the central groove with $\lambda = \lambda_0$.

In the example structures mentioned previously, we find that the determination of the matrix $(R^H - R^W)$ on the left-hand side of Eq. (3) can take near-zero values for some special set of $\{l_j\}$, which means the amplitude H^+ in the passive waveguides can have a nontrivial solution even without any independent inputs ($A^+ = 0$). These nontrivial solutions coincide with the definition of a BIC because they can only exist as bound states near the surface. In the following, we adapt our method to design a BIC system with a similar structure.

As shown schematically in Fig. 5(a), we consider a structure with a number of grooves carved on the planar sound-hard surface. In principle, a BIC could exist on the surface because the radiation from the grooves can cancel each other by multiple interference when the waves from different grooves have a proper phase difference. To determine the phase difference, or say, to determine the depth of the grooves, we modify the structure as a multiport system by extending the far end of the grooves as endless waveguides. By selecting one of the waveguides as the main waveguide and denoting the wave amplitude in it as $A^{\pm}$, and treating the others as subwaveguides and denoting the wave amplitude in them as $H^{\pm}$, respectively, where the superscript + (−) means the wave into (away from) the surface, we can calculate numerically the matrices R^A, T^A, R^H, and T^H using a procedure similar to those performed in the previous examples. With these matrices, the absolute value of A^- can be maximized by optimizing the ending length l_j ($j = 1, \ldots, N$) of the subwaveguides using Eqs. (1) and (3) for the given A^+.

For simplicity, we restrict the width of all waveguides to be the same and be smaller than $\lambda_0/2$, under which only the zeroth waveguide mode can exist. With this simplification, the amplitude vectors $A^{\pm}$ and $H_j^{\pm}$ ($j = 1, \ldots, N$) become scalar quantities. To find a BIC structure based on this configuration, we can search for the $\{l_j\}$ set with the target function $|r_0| = |A^-/A^+| = 1$, which means the incident energy from the far end of the main waveguide is totally reflected back, or say, no wave energy can radiate away in the upper half-infinite space. After $\{l_j\}$ is determined, the ending length of the main waveguide l_0 can then be determined by $l_0 = (\theta_{r_0}/2\pi)\lambda_0$, where θ_{r_0} is the phase of r_0.

In our design, systems with the same and fixed wall thickness $t_w = 0.05\lambda_0$ but with different widths of the waveguide t_g are checked. Numerical results show that, for a given t_g, the target $|r_0| \to 1$ can always be satisfied when the number of grooves N becomes large enough. For example, for $t_g = 0.2\lambda_0$, the $\{l_j\}$ ($j = 0, 1, \ldots, N$) set with the target of $|r_0| < 10^{-6}$ can be found when $N \geq 9$, while for $t_g = 0.3\lambda_0$, the $\{l_j\}(j = 0, 1, \cdots, N)$ set with the same target can be found when $N \geq 13$, and when t_g increases to $0.4\lambda_0$, $N \geq 37$ is necessary for the same target.

As a demonstration, we show the results in Figs. 5(b)–5(d) for the obtained structure with $t_g = 0.4\lambda_0$ and $N = 37$. Shown in Fig. 5(b) is the optimized depth of the grooves for the structure. It can be seen that the structure is symmetric about its central groove. Notice that the optimization value for the ending length of the waveguide l_j ($j = 0, \ldots, N$) may be very small; if this happens, we need to set them as $l_j + (\lambda_0/2)$ to let the near field at the opening of the waveguide be undisturbed. To verify the BIC in the structure, we calculate $|r_0|^2$ as a function of the wavelength λ/λ_0, where λ is the wavelength of the incident wave in free space, and the result is shown in Fig. 5(c). For the figure, we inject a plane wave from the central groove [marked by a red arrow in Fig. 5(b)] and set at the same time its bottom as the plane-wave radiation boundary. It can be seen from the figure that $|r_0|^2$ takes a near unity value at $\lambda/\lambda_0 = 1$, which means there is negligible radiation in the upper half-infinite space. Shown in Fig. 5(d) is the total field distribution for the amplitude of the pressure wave for incidence with $\lambda/\lambda_0 = 1$, from which the bounding feature of the mode can be clearly seen.

IV. CONCLUSION

In conclusion, we introduce a multiport structural model to describe the wave scattering behavior of a metasurface. Using the model, we understand that, as the output mode in each port is the superposition of the scattered waves excited by the inputs from all involved ports, the field in space can be customized by adjusting the inputs from the ports. Based on this understanding, a design method for a nonlocal metastructure is suggested and four metastructures with different kinds of target field are designed as illustrations. Results show that the method has good adaptability for structures with various targets and is efficient enough for complex structures with a large number of constructive units. Moreover, because the scattering matrix of the system, which is the basis of the metastructure design, can be obtained by a numerical simulation procedure or even by experimental measurement, the method should be valid for structures with arbitrary configurations and in complicated environments. This is useful when we need to design structures with target field distributions in complex media or in space with irregular boundaries, such as in organic tissue, in architectural structures, or other situations. It can be also found that the suggested model gives not only a design method, but also an alternative understanding for metastructures, based on which more comprehensive metastructures can be conceived.

ACKNOWLEDGMENTS

This work was supported by the National Natural Science Foundation of China (Grant No. 12274143).

[1] B. Assouar, B. Liang, Y. Wu, Y. Li, J.-C. Cheng, and Y. Jing, Acoustic metasurfaces, Nat. Rev. Mater. **3**, 460 (2018).

[2] J. Mei and Y. Wu, Controllable transmission and total reflection through an impedance-matched acoustic metasurface, New J. Phys. **16**, 123007 (2014).

[3] K. Tang, C. Qiu, M. Ke, J. Lu, Y. Ye, and Z. Liu, Anomalous refraction of airborne sound through ultrathin metasurfaces, Sci. Rep. **4**, 6517 (2014).

[4] Y. Li, B. Liang, Z. M. Gu, X. Y. Zou, and J. C. Cheng, Reflected wavefront manipulation based on ultrathin planar acoustic metasurfaces, Sci. Rep. **3**, 2546 (2013).

[5] Y. Li, C. Shen, Y. Xie, J. Li, W. Wang, S. A. Cummer, and Y. Jing, Tunable asymmetric transmission via lossy acoustic metasurfaces, Phys. Rev. Lett. **119**, 035501 (2017).

[6] X. Jiang, B. Liang, X. Y. Zou, J. Yang, L. L. Yin, J. Yang, and J. C. Cheng, Acoustic one-way metasurfaces: Asymmetric phase modulation of sound by subwavelength layer, Sci. Rep. **6**, 28023 (2016).

[7] Y. Fu, Y. Tian, X. Li, S. Yang, Y. Liu, Y. Xu, and M. Lu, Asymmetric generation of acoustic vortex using dual-layer metasurfaces, Phys. Rev. Lett. **128**, 104501 (2022).

[8] J. Chen, J. Xiao, D. Lisevych, A. Shakouri, and Z. Fan, Deep-subwavelength control of acoustic waves in an ultra-compact metasurface lens, Nat. Commun. **9**, 4920 (2018).

[9] H. Taghvaee, F. Liu, A. Díaz-Rubio, and S. Tretyakov, Perfect-lens theory enables metasurface reflectors for subwavelength focusing, Phys. Rev. Appl. **19**, 014004 (2023).

[10] J. Mei, Lijuan Fan, and Xiaobin Hong, Broadband and high-numerical-aperture sharp focusing for waterborne sound with metagrating-based lens, New J. Phys. **24**, 093014 (2023).

[11] H. Esfahlani, S. Karkar, H. Lissek, and J. R. Mosig, Acoustic carpet cloak based on an ultrathin metasurface, Phys. Rev. B **94**, 014302 (2016).

[12] Y. Jin, X. Fang, Y. Li, and D. Torrent, Engineered diffraction gratings for acoustic cloaking, Phys. Rev. Appl. **11**, 011004 (2019).

[13] H. Xie and Z. Hou, Nonlocal metasurface for acoustic focusing, Phys. Rev. Appl. **15**, 034054 (2021).

[14] Y. Xie, C. Shen, W. Wang, J. Li, D. Suo, B. I. Popa, Y. Jing, and S. A. Cummer, Acoustic holographic rendering with two-dimensional metamaterial-based passive phased array, Sci. Rep. **6**, 35437 (2016).

[15] K. Melde, A. G. Mark, T. Qiu, and P. Fischer, Holograms for acoustics, Nature **537**, 518 (2016).

[16] N. Yu, P. Genevet, M. A. Kats, F. Aieta, J. P. Tetienne, F. Capasso, and Z. Gaburro, Light propagation with phase discontinuities: Generalized laws of reflection and refraction, Science **334**, 333 (2011).

[17] A. Díaz-Rubio and S. A. Tretyakov, Acoustic metasurfaces for scattering-free anomalous reflection and refraction, Phys. Rev. B **96**, 125409 (2017).

[18] V. S. Asadchy, M. Albooyeh, S. N. Tcvetkova, A. Díaz-Rubio, Y. Ra'di, and S. A. Tretyakov, Perfect control of reflection and refraction using spatially dispersive metasurfaces, Phys. Rev. B **94**, 075142 (2016).

[19] Y. Ra'di, D. L. Sounas, and A. Alù, Metagratings: Beyond the limits of graded metasurfaces for wave front control, Phys. Rev. Lett. **119**, 067404 (2017).

[20] Z. Hou, X. Fang, Y. Li, and B. Assouar, Highly efficient acoustic metagrating with strongly coupled surface grooves, Phys. Rev. Appl. **12**, 034021 (2019).

[21] H. Ni, X. Fang, Z. Hou, Y. Li, and B. Assouar, High-efficiency anomalous splitter by acoustic meta-grating, Phys. Rev. B **100**, 104104 (2019).

[22] A. Epstein and G. V. Eleftheriades, Synthesis of passive lossless metasurfaces using auxiliary fields for

reflectionless beam splitting and perfect reflection, Phys. Rev. Lett. **117**, 256103 (2016).

[23] A. Diaz-Rubio, J. Li, C. Shen, S. A. Cummer, and S. A. Tretyakov, Power flow-conformal metamirrors for engineering wave reflections, Sci. Adv. **5**, eaau7288 (2019).

[24] L. Fan and J. Mei, Metagratings for waterborne sound: Various functionalities enabled by an efficient inverse-design approach, Phys. Rev. Appl. **14**, 044003 (2020).

[25] S. Cao and Z. Hou, Angular-asymmetric transmitting metasurface and splitter for acoustic waves: Combining the coherent perfect absorber and a laser, Phys. Rev. Appl. **12**, 064016 (2019).

[26] J. Zhu, X. Zhu, X. Yin, Y. Wang, and X. Zhang, Unidirectional extraordinary sound transmission with mode-selective resonant materials, Phys. Rev. Appl. **13**, 041001 (2020).

[27] Y. Xu, C. Gu, B. Hou, Y. Lai, J. Li, and H. Chen, Broadband asymmetric waveguiding of light without polarization limitations, Nat. Commun. **4**, 2561 (2013).

[28] W. K. Cao, L. T. Wu, C. Zhang, J. C. Ke, Q. Cheng, T. J. Cui, and Y. Jing, Asymmetric transmission of acoustic waves in a waveguide via gradient index metamaterials, Sci. Bull. (Beijing) **64**, 808 (2019).

[29] H. Wang, Y. Xu, P. Genevet, J. H. Jiang, and H. Chen, Broadband mode conversion via gradient index metamaterials, Sci. Rep. **6**, 24529 (2016).

[30] F. Ma, Z. Huang, C. Liu, and J. H. Wu, Acoustic focusing and imaging via phononic crystal and acoustic metamaterials, J. Appl. Phys. **131**, 011103 (2022).

[31] Y. K. Chiang, L. Quan, Y. Peng, S. Sepehrirahnama, S. Oberst, A. Alù, and D. A. Powell, Scalable metagrating for efficient ultrasonic focusing, Phys. Rev. Appl. **16**, 064014 (2021).

[32] C. Zhou, X. Qu, S. Xiao, and M. Fan, Imaging through a Fano-resonant dielectric metasurface governed by quasi–bound states in the continuum, Phys. Rev. Appl. **14**, 044009 (2020).

[33] S. Huang, T. Liu, Z. Zhou, X. Wang, J. Zhu, and Y. Li, Extreme sound confinement from quasibound states in the continuum, Phys. Rev. Appl. **14**, 021001 (2020).

[34] M. McIver, Trapped modes supported by submerged obstacles, Proc. R. Soc. A **456**, 1851 (2000).

[35] L. Cao, Y. Zhu, S. Wan, Y. Zeng, Y. Li, and B. Assouar, Perfect absorption of flexural waves induced by bound state in the continuum, Extreme Mech. Lett. **47**, 101364 (2021).

[36] C. W. Hsu, B. Zhen, A. D. Stone, J. D. Joannopoulos, and M. Soljačić, Bound states in the continuum, Nat. Rev. Mater. **1**, 16048 (2016).

[37] S. I. Azzam and A. V. Kildishev, Photonic bound states in the continuum: From basics to applications, Adv. Opt. Mater. **9**, 2001469 (2020).